

9. K. Sieh, *Philos. Trans. R. Soc. London Ser. A* **364**, 1947 (2006).
10. K. Sieh, paper presented at the First International Conference of Aceh and Indian Ocean Studies, Banda Aceh, Indonesia, 24 to 26 February 2007.
11. K. Sieh, *J. Earthquake Tsunami* **1**, 1 (2007).
12. O. Konca *et al.*, *Nature* **456**, 631 (2008).
13. J. Zachariassen, K. Sieh, F. W. Taylor, R. L. Edwards, W. S. Hantoro, *J. Geophys. Res.* **104**, 895 (1999).
14. J. Zachariassen, K. Sieh, F. W. Taylor, W. S. Hantoro, *Bull. Seismol. Soc. Am.* **90**, 897 (2000).
15. D. H. Natawidjaja *et al.*, *J. Geophys. Res.* **109**, B04306 (2004).
16. D. R. Stoddart, T. P. Scoffin, *Atoll Res. Bull.* **224**, 1 (1979).
17. C. Darwin, *The Structure and Distribution of Coral Reefs* (Smith, Elder and Co., London, 1842).
18. R. L. Edwards, F. W. Taylor, G. J. Wasserburg, *Earth Planet. Sci. Lett.* **90**, 371 (1988).
19. C.-C. Shen *et al.*, *Geochim. Cosmochim. Acta* **72**, 4201 (2008).
20. C.-C. Shen *et al.*, *Chem. Geol.* **185**, 165 (2002).
21. We use the terms "submergence" and "emergence" throughout to refer to changes with respect to a sea-level datum. We use "subsidence" and "uplift" in reference to other geodetic data and when inferring vertical tectonic motions.
22. K. Sieh, *Nature* **434**, 573 (2005).
23. Y.-J. Hsu *et al.*, *Science* **312**, 1921 (2006).
24. K. Sieh, M. Stuiver, D. Brillinger, *J. Geophys. Res.* **94**, 603 (1989).
25. G. Carver *et al.*, *Bull. Seismol. Soc. Am.* **94**, S58 (2004).
26. J. C. Borrero, K. Sieh, M. Chlieh, C. E. Synolakis, *Proc. Natl. Acad. Sci. U.S.A.* **103**, 19673 (2006).
27. This work has been supported by NSF grants EAR-9628301, 9804732, 9903301, 0208508, 0530899, 0538333, and 0809223 (to K.S.) and EAR-0207686

and 0537973 (to R.L.E.); by National Science Council grants 94-2116-M002-012 and 95&96-2752-M002-012-PAE (to C.-C.S.); by LIPI (Indonesian Institute of Science) and RUTI (International Joint Research Program of the Indonesian Ministry of Research and Technology); and by the Gordon and Betty Moore Foundation. This is Caltech Tectonics Observatory contribution number 86 and Earth Observatory of Singapore contribution number 1.

Supporting Online Material

www.sciencemag.org/cgi/content/full/322/5908/1674/DC1
SOM Text
Figs. S1 to S44
Tables S1 to S4
References

22 July 2008; accepted 8 October 2008
10.1126/science.1163589

Shock Metamorphism of Bosumtwi Impact Crater Rocks, Shock Attenuation, and Uplift Formation

Ludovic Ferrière,¹ Christian Koeberl,^{1*} Boris A. Ivanov,² Wolf Uwe Reimold³

Shock wave attenuation rate and formation of central uplifts are not precisely constrained for moderately sized complex impact structures. The distribution of shock metamorphism in drilled basement rocks from the 10.5-kilometer-diameter Bosumtwi crater, and results of numerical modeling of inelastic rock deformation and modification processes during uplift, constrained with petrographic data, allowed reconstruction of the pre-impact position of the drilled rocks and revealed a shock attenuation by ~5 gigapascals in the uppermost 200 meters of the central uplift. The proportion of shocked quartz grains and the average number of planar deformation feature sets per grain provide a sensitive indication of minor changes in shock pressure. The results further imply that for moderately sized craters the rise of the central uplift is dominated by brittle failure.

During the contact and compression phase of hypervelocity impact, a spherical shock wave is generated, propagates through the target rocks (*1*), and is attenuated rapidly with increasing distance. Consequently, a variety of shock effects are produced in rock-forming minerals, including formation of planar deformation

features (PDFs) and high-pressure phases. The relative spatial distribution of these shock transformations and deformations formed at different pressures and temperatures [e.g., (*2*, *3*)] in autochthonous rocks, at the scale of the impact structure, can be used to estimate maximum shock pressures and, consequently, the rate of shock attenuation.

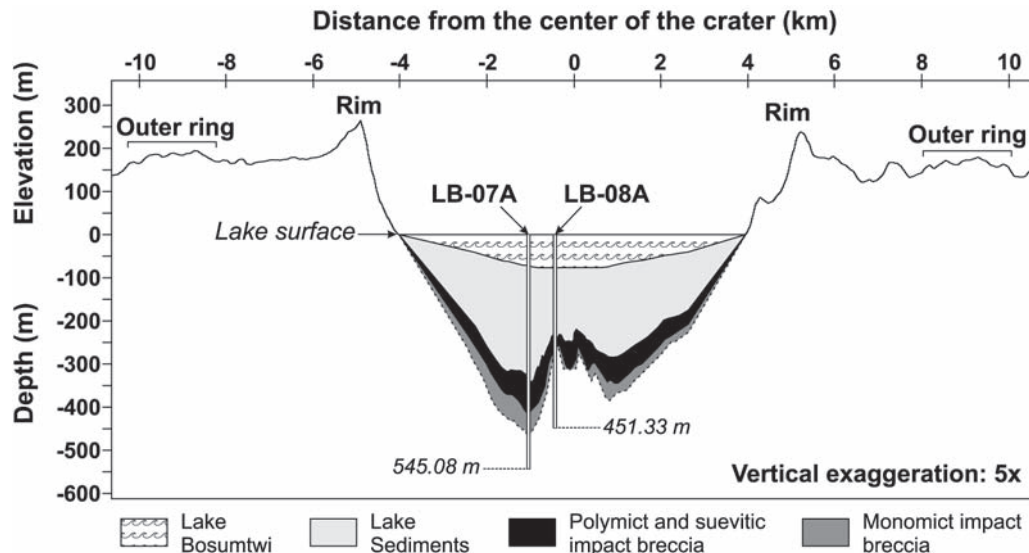
However, many parameters—such as rock type as well as lithological contrasts, texture, fabric, grain size, preshock orientation of grains, porosity, and volatile content—influence the shock levels attained locally. Furthermore, and typical in the case of complex impact structures (i.e., craters with diameters ≥ 2 to 4 km on Earth) (*4*), the original position and distribution of the shocked rocks is modified when, because of gravitational instability of the transient cavity rim, rebound of the crater floor leads to formation of a central uplift. Redistribution of rock is also associated with the collapse of the initially oversteepened central uplift (*5*).

There have been several efforts to estimate shock wave decay, mainly from nuclear and explosion crater studies or by numerical modeling [e.g., (*6–8*)]. Few studies have tried to quantify shock pressure distribution in simple (*9*) and complex impact structures (*9–16*) [see supporting

¹Department of Lithospheric Research, University of Vienna, Althanstrasse 14, A-1090 Vienna, Austria. ²Institute for Dynamics of Geospheres, Russian Academy of Sciences, Leninsky Prospect 38-1, 119334 Moscow, Russia. ³Museum of Natural History (Mineralogy), Humboldt University, Invalidenstrasse 43, D-10115 Berlin, Germany.

*To whom correspondence should be addressed. E-mail: christian.koeberl@univie.ac.at

Fig. 1. Cross section of the Bosumtwi impact structure, based on Shuttle Radar Topography Mission (SRTM) data for the regional topography of the exposed portion of the crater (profile from west to east) and on a northwest-southeast seismic reflection profile (*21*) across the central crater. Location of boreholes LB-07A and LB-08A are given. The volume of lake sediments is based on seismic reflection data. The distribution of polymict and suevitic impact breccia and monomict impact breccia is based on observations from cores LB-07A and LB-08A (*19*, *20*), as well as interpretations of seismic reflection data. Depths and elevations are relative to lake level. SRTM data were available online (www2.jpl.nasa.gov/srtm/; accessed 3 March 2008).



online material (SOM text)] by using the frequency of shock-induced deformations in quartz grains from samples taken along profiles across the erosion surface of an impact structure. Only three investigations have explored the relative vertical decay of recorded shock pressure in complex impact structures, two for the ~40-km-diameter Puchezh-Katunki impact structure (13, 15) and another for the ~65-km-diameter Kara crater (11).

We characterized the shock wave attenuation in the uppermost part of the central uplift of the Bosumtwi impact structure, a moderately sized (10.5-km diameter) and well-preserved complex impact structure [e.g., (17)], and attempted to reconstruct the original position of the sampled section in the target before crater modification. This is possible by combining petrographic investigations (at the microscale) with modeling of inelastic rock deformation (at the mesoscale) and modification processes during uplift (at the megascale). This approach allows us to constrain shock wave attenuation and rock deformation during central uplift formation.

We studied drill core samples from the central part of the structure retrieved in the 2004 International Continental Scientific Drilling Program (ICDP) Bosumtwi drilling project (18–20) (SOM text). The central uplift extends ~130 m above the crater moat, is ~1.9 km wide (21), and is composed of metasedimentary rocks [mostly metagraywacke (MGW) and shale] (19). Two cores were retrieved by the ICDP project: core LB-08A from the outer flank of the central uplift and core LB-07A from the deep crater moat (Fig. 1 and SOM text).

To derive the distribution of shock metamorphic effects with depth, we studied 18 MGW samples from 271.4- to 451.2-m depth in core LB-08A (Fig. 1), recording modal analysis and shock deformation properties of 8991 quartz grains (22) (tables S1 and S2). We determined 1056 crystallographic orientations of sets of PDFs in 602 quartz grains (table S3) because predominance of specific orientations of PDFs in quartz has long been considered to indicate different shock pressures [e.g., (23)].

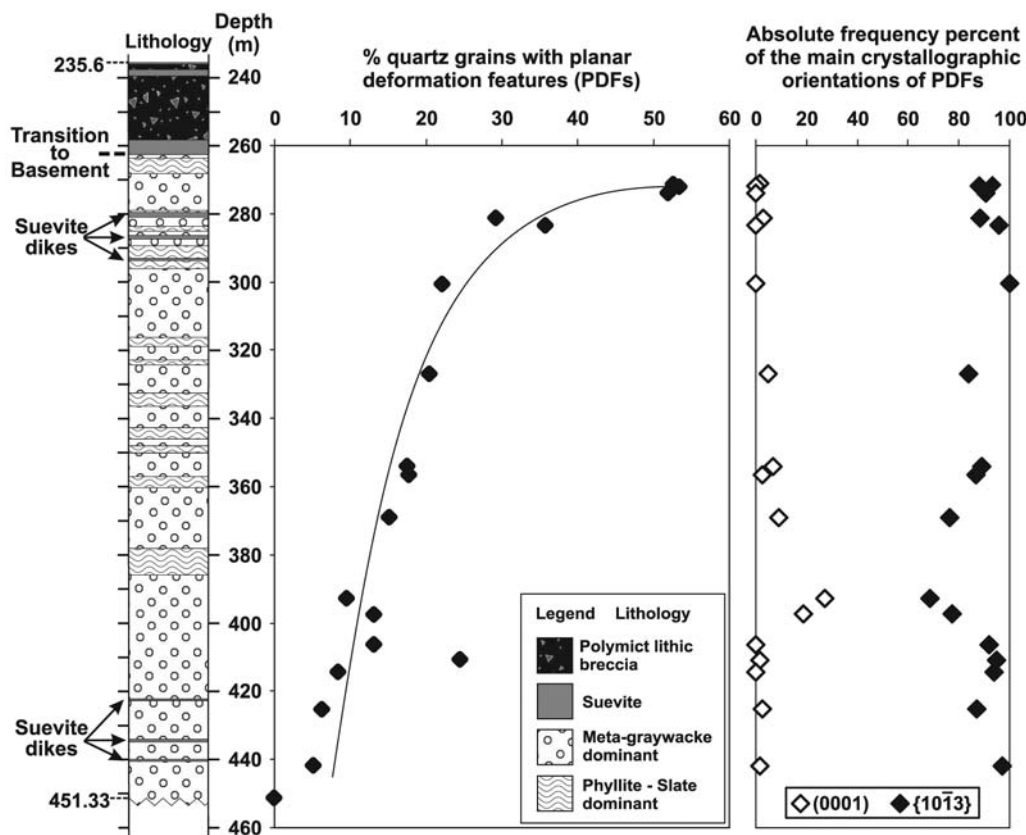
The abundance of shocked quartz grains (i.e., quartz grains with planar fractures and/or PDFs) decreases with increasing depth (for PDFs, compare with Fig. 2). We interpret this decrease to reflect the variation of shock pressure in the uppermost part of the central uplift. Similarly, the average number of PDF sets per quartz grain (N) decreases steadily with depth, from ~2.1 at 271-m depth to ~1.6 at 442 m (Fig. 3). We interpret the decrease of N as evidence of the shock pressure attenuation with distance from shock wave origin.

No clear change was evident over this interval in the relative frequencies of the main crystallographic orientations of PDF sets in quartz grains with increasing depth (Fig. 2 and table S3). Most of the poles to the PDF planes correspond to the $\omega\{10\bar{1}3\}$ orientation, and only a few, typically less than 5 relative-percent (rel%) of the orientation data obtained per section, correspond to basal [i.e., parallel to (0001)] planes. Only two samples, KR8-85 and KR8-89, from 390- to 400-m depth, show a higher proportion of basal PDF, at about 27 and 19 rel%, respectively (table S3).

These two MGW samples originated just below a 10-m-thick layer of comparatively fine-grained metasedimentary rocks (phyllite and slate; Fig. 2); thus, it is possible that shock wave interference at the transition from metapelite to MGW resulted in the local formation of a larger proportion of basal PDFs [basal PDFs are formed at lower pressures (from 8 to 10 GPa) than $\omega\{10\bar{1}3\}$ orientations (>10 GPa); e.g., (2)]. However, about 50% of the basal PDFs measured in these two samples occur in association with $\omega\{10\bar{1}3\}$ PDF (i.e., dual sets of PDFs in the same quartz grain), which indicates relatively high shock pressures. Thus, minor variations of the relative proportions of crystallographic orientations of PDF sets in quartz grains with depth cannot be used to quantify the slight attenuation of the shock pressure along the ~200-m-long bedrock section investigated here. Because the relative proportion of shocked quartz grains, as well as the number of PDF sets per quartz grain, steadily decrease with depth (Figs. 2 and 3), we infer that the shock wave was attenuated but not by much.

On the basis of the relative abundances of quartz grains with PDFs, the presence of multiple sets of PDFs in quartz grains (up to four sets), and the occurrence of various PDF set orientations, we estimate that the studied section experienced peak shock pressures of up to ~25 to 30 GPa [e.g., (2, 24–25)]. The upper limit of peak shock pressure (i.e., 30 GPa) is further constrained by the lack of isotropization of the quartz grains, which typically begins at this shock pressure [e.g., (2)]. The estimated pressure range is much too low for either

Fig. 2. Simplified lithostratigraphic column for drill core LB-08A [after (19)] and PDF data for 18 MGW samples from the basement section. The abundance of quartz grains with PDFs relative to the total number of quartz grains is shown (left, solid diamond) and, on the right, the absolute frequency percent of the two main PDF crystallographic orientations (open diamond symbols for basal PDF and solid diamonds for $\omega\{10\bar{1}3\}$ crystallographic orientation data) in quartz grains, as measured on a universal stage.



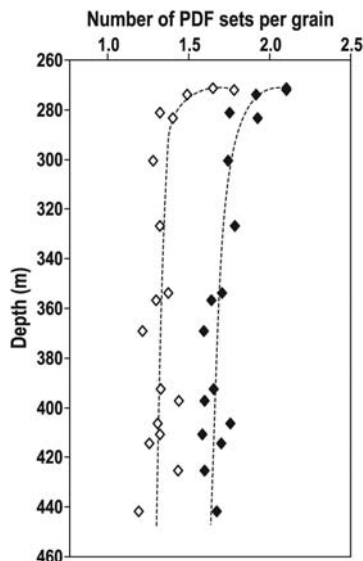


Fig. 3. Average number of PDF sets per host quartz grain (N) in MGW samples from the uppermost ~200 m of basement drilled in the central uplift of the Bosumtwi impact structure. For both methods, that is, with use of a petrographic microscope (under horizontal stage examination; open diamonds) and with the U stage (solid diamonds), N values follow the same trend of decreasing abundance of PDF sets per grain with increasing depth.

partial or total shock melting of the whole rock, which is in agreement with macroscopic and microscopic observations on these metasedimentary rocks that have preserved their preimpact texture (19) (SOM text). Thus, the rise of the central uplift was not facilitated by shock-induced plasticity, and brittle failure was dominant. This finding is also supported by the presence of abundant faults in the central uplift, as indicated by reflection seismic data (21).

To further evaluate the apparent shock attenuation, we calculated the expected shock pressure attenuation and reconstructed the preimpact position of the investigated section of the central uplift by numerical modeling, by using a variant of the SALEB numerical code (26) (SOM text). To model the crater and central uplift properly, we did a direct parametric fit of our model to the observed crater geometry without usage of scaling relations for the crater size (SOM text and fig. S3). After modeling, tracers in the vicinity of the exact location of the two drill holes were identified (allowing the tracking of their initial positions), and lastly the position of the top of the “model core” was defined by the maximum recorded shock pressure of 30 GPa (based on our petrographic investigations). Then, the initial position of these tracers was plotted (Fig. 4). Our calculations show that, despite quite similar present-day depths, the initial depth of rocks in the crater moat (core LB-07A) was above that of the rocks in the central uplift corehole (Fig. 4). This specific displacement of the target rocks during crater modification is interesting because it indicates that rocks occurring in the outer flank of the central uplift

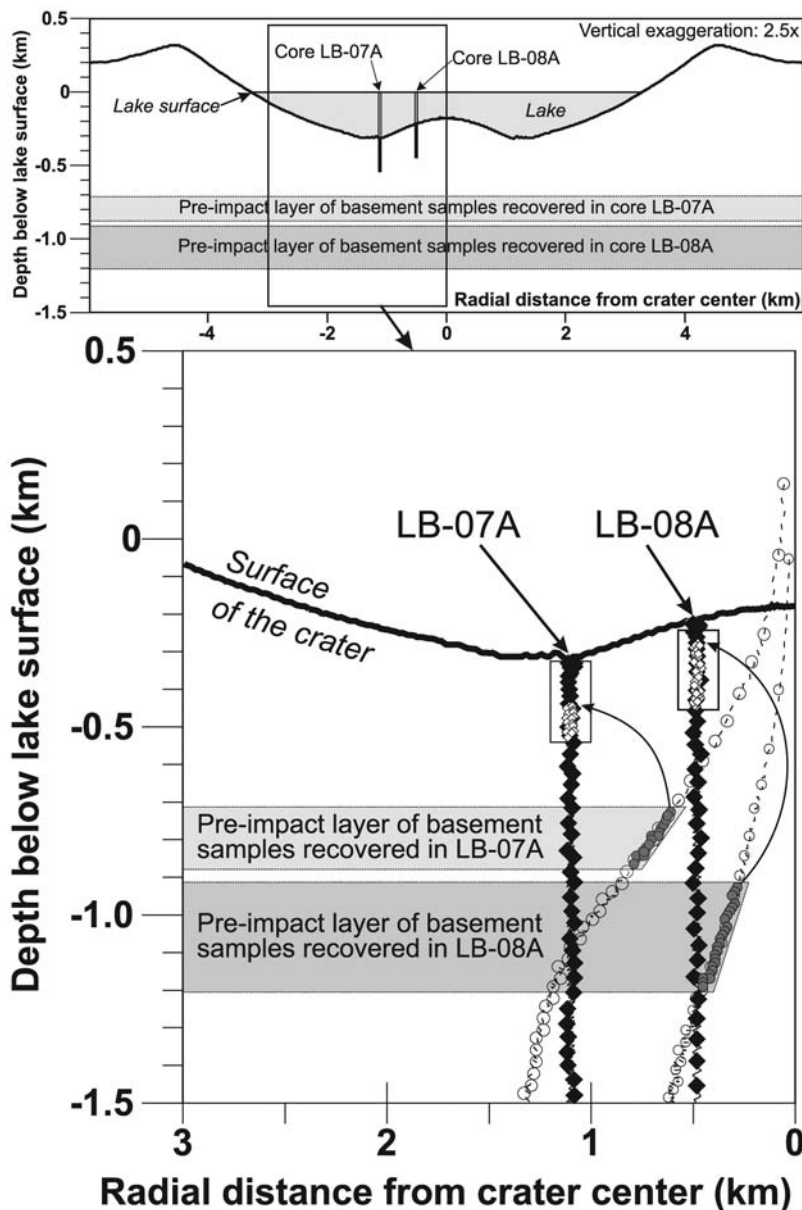


Fig. 4. Calculated crater profile with enlarged inner part showing initial and final positions of rocks recovered in drill cores LB-07A (from the crater moat) and LB-08A (from the outer flank of the central uplift). Solid diamonds show final positions of tracers (0.48- and 1.1-km radial distance from crater center), whereas open circles indicate their initial positions in the preimpact target stratigraphy. Gray dots and open diamonds show, respectively, the initial and the final positions of basement samples (i.e., investigated MGW samples in core LB-08A) recovered in drill cores. Solid diamonds above open diamonds represent the modeled impact breccia. Locations of drill cores are indicated by large open rectangles. Model run with ANEOS (analytical equation of state) granite (28), an impact velocity of 20 km^{-1} , and a residual friction (μ) of 0.4. For comparison of the calculated and the actual cross sections of the Bosumtwi crater, see fig. S3.

were originally more deeply buried than the basement rocks drilled below the deep crater moat and, thus, were subjected to somewhat lower shock pressures. Thus, before estimating shock attenuation in complex impact structures, it is important to consider the differential movements of the target rocks, which cause changes in the spherical shock-attenuation scheme. The numerical model (Fig. 4 and SOM text) indicates that the samples investigated in core LB-08A have

been uplifted by about 1.2 to 1.5 km. By using the relationship $SU = 0.086D^{1.03}$ (27) (where D is the crater diameter), we estimated the amount of structural uplift (SU) for the Bosumtwi central uplift at about 1 km, in good agreement with the modeling result.

Taking into account the uplift of target rocks, the calculated apparent shock attenuation along the about-200 m of investigated core is ~5 to 10 GPa (fig. S4). On the basis of the general absence of

changes in the statistics of PDF orientations, a maximum shock attenuation of 5 GPa seems to be the more realistic value.

The percentage of shocked quartz grains and the number of PDF sets per grain are more sensitive indicators of minor changes in shock pressure than pure PDF orientation statistics. The combination of detailed petrographic investigation and numerical modeling indicates that both of these approaches are essential to reconstruct the preimpact position of rocks and to characterize properly the shock pressure distribution at the scale of an impact structure. Our observations suggest that, in the case of the 10.5-km-diameter Bosumtwi impact structure, the uppermost rocks of the central uplift experienced shock pressures below 30 GPa, whereas pressures up to 40 to 45 GPa were recorded for the about-four-times-larger Puchezh-Katunki impact structure (15). Shock attenuation in the uppermost part of a central uplift has been, for the first time, constrained by detailed shock degree profiling at the microscale. Numerical modeling of this section of the central uplift has then established where this section of the central uplift was located before uplift formation, which was only possible once the shock regime had been established by micropetrography. The results imply that, for moderately sized impact craters, the rise of the central uplift is dominated by brittle failure, whereas in the case of larger impact structures, and also depending on rock properties, the uplifted, relatively stronger shocked rocks may behave in a more ductile manner.

References and Notes

1. D. Stöffler, *Fortschr. Mineral.* **49**, 50 (1972).
2. D. Stöffler, F. Langenhorst, *Meteorit. Planet. Sci.* **29**, 155 (1994).
3. R. A. F. Grieve, F. Langenhorst, D. Stöffler, *Meteorit. Planet. Sci.* **31**, 6 (1996).
4. R. A. F. Grieve, *Annu. Rev. Earth Planet. Sci.* **15**, 245 (1987).
5. H. J. Melosh, *Impact Cratering: A Geological Process* (Oxford Univ. Press, New York, 1989).
6. J. T. Cherry, F. L. Petersen, in *Peaceful Nuclear Explosions* (International Atomic Energy Agency, Vienna, 1970), pp. 241–325.
7. T. J. Ahrens, J. D. O'Keefe, in *Impact and Explosion Cratering*, D. J. Roddy, R. O. Pepin, R. B. Merrill, Eds. (Pergamon, New York, 1977), pp. 639–656.
8. N. K. Mitani, *J. Geophys. Res.* **108**, 5003 (2003).
9. P. B. Robertson, R. A. F. Grieve, in *Impact and Explosion Cratering*, D. J. Roddy, R. O. Pepin, R. B. Merrill, Eds. (Pergamon, New York, 1977), pp. 687–702.
10. R. A. F. Grieve, P. B. Robertson, *Contrib. Mineral. Petrol.* **58**, 37 (1976).
11. L. V. Sazonova, N. N. Karotaeve, G. Y. Ponomarev, A. I. Dabizha, in *Impactites*, A. A. Marakushev, Ed. (Moscow State Univ., Moscow, 1981), pp. 93–133.
12. R. A. F. Grieve, J. M. Coderre, P. B. Robertson, J. Alexopoulos, *Tectonophysics* **171**, 185 (1990).
13. V. I. Fel'dman, L. V. Sazonova, S. I. Kotel'nikov, *Dokl. Akad. Nauk SSSR* **349**, 658 (1996).
14. B. O. Dressler, V. L. Sharpton, B. C. Schuraytz, *Contrib. Mineral. Petrol.* **130**, 275 (1998).
15. V. L. Masaitis, L. A. Pevzner, *Deep Drilling in the Impact Structure: Puchezh-Katunki, Russia* (VSEGEI, St. Petersburg, 1999).
16. R. L. Gibson, W. U. Reimold, *Geol. Soc. Am. Spec. Pap.* **384**, 329 (1996).
17. C. Koeberl, W. U. Reimold, *Yearb. Austrian Geol. Surv.* **145**, 31 (2005).
18. C. Koeberl *et al.*, *Meteorit. Planet. Sci.* **42**, 483 (2007).
19. L. Ferrière, C. Koeberl, W. U. Reimold, *Meteorit. Planet. Sci.* **42**, 611 (2007).
20. L. Coney, R. L. Gibson, W. U. Reimold, C. Koeberl, *Meteorit. Planet. Sci.* **42**, 569 (2007).
21. C. A. Scholz *et al.*, *Geology* **30**, 939 (2002).
22. Materials and methods are available as supporting material on Science Online.
23. F. Hörz, in *Shock Metamorphism of Natural Materials*, B. M. French, N. M. Short, Eds. (Mono, Baltimore, 1968), pp. 243–253.
24. A. R. Huffman, W. U. Reimold, *Tectonophysics* **256**, 165 (1996).
25. B. M. French, *Traces of Catastrophe: A Handbook of Shock-Metamorphic Effects in Terrestrial Meteorite Impact Structures* [LPI Contribution No. 954, Lunar and Planetary Institute (LPI), Houston, TX, 1998].
26. B. Ivanov, *Sol. Syst. Res.* **39**, 381 (2005).
27. M. J. Cintala, R. A. F. Grieve, *Meteorit. Planet. Sci.* **33**, 889 (1998).
28. E. Pierazzo, A. M. Vickery, H. J. Melosh, *Icarus* **127**, 408 (1997).
29. Drilling was funded by ICDP, NSF, the Austrian Fonds zur Förderung der wissenschaftlichen Forschung (FWF), the Canadian Natural Sciences and Engineering Research Council, and the Austrian Academy of Sciences. We thank DOSECC (Drilling, Observation and Sampling of the Earth's Continental Crust) for the drilling operations. This work was supported by the Austrian FWF (grants P17194-N10 and P18862-N10) and the Austrian Academy of Sciences. B.A.I. was supported by the Russian Foundation for Basic Science (RFBR grant 08-05-00908-a), and W.U.R.'s research is supported by the German Science Foundation (Deutsche Forschungsgemeinschaft) and Humboldt University of Berlin.

Supporting Online Material

www.sciencemag.org/cgi/content/full/322/5908/1678/DC1
Materials and Methods

SOM Text

Figs. S1 to S4

Tables S1 to S4

References

23 September 2008; accepted 10 November 2008
10.1126/science.1166283

The Spreading of Disorder

Kees Keizer,* Siegwart Lindenberg, Linda Steg

Imagine that the neighborhood you are living in is covered with graffiti, litter, and unreturned shopping carts. Would this reality cause you to litter more, trespass, or even steal? A thesis known as the broken windows theory suggests that signs of disorderly and petty criminal behavior trigger more disorderly and petty criminal behavior, thus causing the behavior to spread. This may cause neighborhoods to decay and the quality of life of its inhabitants to deteriorate. For a city government, this may be a vital policy issue. But does disorder really spread in neighborhoods? So far there has not been strong empirical support, and it is not clear what constitutes disorder and what may make it spread. We generated hypotheses about the spread of disorder and tested them in six field experiments. We found that, when people observe that others violated a certain social norm or legitimate rule, they are more likely to violate other norms or rules, which causes disorder to spread.

In the mid-1990s, the mayor of New York and his police commissioner adopted a "Quality of life campaign." Attention was focused on fighting signs of disorder and petty crime. Graffiti was removed, streets were swept, and signs of vandalism were cleared. This initiative was based on the broken windows theory (BWT) of Wilson and Kelling (1). The BWT suggests that signs of

disorder like broken windows, litter, and graffiti induce other (types of) disorder and petty crime (2). It was thought that removing these signs of disorder would take away an important trigger of disorderly and petty criminal behavior. After the introduction of the campaign, petty crime rates in New York dropped. Since then, approaches based on the BWT have become popular and have been adopted worldwide (e.g., in various cities in the United States, Great Britain, Netherlands, Indonesia, and South Africa).

BWT may be very popular, but it is also highly controversial. So far, it lacks empirical

support, and it fails to specify what constitutes disorder. Studies aimed to test the BWT (3–6) have provided mixed results at best. The National Research Council (NRC) concluded that the research did not provide strong support for the BWT (7). There is also little evidence that broken window policing contributed to the sharp decrease in petty crime in New York (8–10). Moreover, to our knowledge, research on the BWT has so far been correlational, so conclusions about causality are shaky (6, 8). The BWT suggests that a setting with disorder triggers disorderly and petty criminal behavior, but it might be the other way around or both may be caused by a third variable. Furthermore, the BWT gives no insight into what is and what is not a condition of disorder that will spread. Because the BWT forms the backbone of many cities' defense against the growing threat of disorder and petty crime, these shortcomings need to be addressed.

In the present study, we conducted six field experiments that address these issues. Our first step was to conceptualize a disorderly setting in such a way that we can link it to a process of spreading norm violations. Social norms refer either to the perception of common (dis)approval of a particular kind of behavior (injunctive norm) or to a particular behavior common in a setting (descriptive norm) (11–16). Injunctive norms affect behavior because they provide information about which behavior is most appropriate in a

Faculty of Behavioral and Social Sciences, University of Groningen, 9712 TS Groningen, Netherlands.

*To whom correspondence should be addressed. E-mail: K.E.Keizer@rug.nl



Supporting Online Material for

Shock Metamorphism of Bosumtwi Impact Crater Rocks, Shock Attenuation, and Uplift Formation

Ludovic Ferrière, Christian Koeberl,* Boris A. Ivanov, Wolf Uwe Reimold

*To whom correspondence should be addressed. E-mail: christian.koeberl@univie.ac.at

Published 12 December 2008, *Science* **322**, 1678 (2008)
DOI: 10.1126/science.1166283

This PDF file includes:

Materials and Methods
SOM Text
Figs. S1 to S4
Tables S1 to S4
References and Notes

Supporting Online Material

Materials and Methods

Eighteen thin sections of meta-graywacke (MGW) samples from the basement rock depth interval from 271.43 m (KR8-029) to 451.23 m (KR8-125) of core LB-08A were prepared. Special attention was paid to avoid significant variation in grain size between the different MGW samples.

The MGW samples are light to dark gray in color and mostly medium-grained (grain size range from ~200 to 600 μm). Note that samples KR8-029, KR8-030, KR8-031, KR8-101, KR8-109, and KR8-119 are relatively coarser-grained, with grain sizes up to a few millimeters. However, these samples do not show any different results from the medium-grained samples, in terms of either abundance of shocked quartz grains or orientation statistics of planar deformation features (PDFs). Most of the MGW samples do not show pre-impact deformation; only a few (KR8-045, KR8-066, KR8-067, and KR8-125) are sheared or display a mylonitic texture (KR8-036, KR8-037, and KR8-071), but these samples do not show any different results from the other samples. Meta-graywacke consists of poorly sorted mineral grains/fragments embedded in a compact matrix mostly composed of very fine-grained secondary minerals, such as chlorite and sericite. Petrographic descriptions of the samples are reported in Ferrière et al. (*S1*); modal analyses are reported in Table S1.

Our investigations were carried out using an optical microscope and a four-axis universal stage (U-stage; cf. *S2*) following three distinct steps:

1) Standard thin-section point counting techniques (e.g., *S3*) were applied to establish quantitative modal compositions. The modal analysis was done by counting ~960 points, on average, per thin section (with a total of 15892 points evaluated for the eighteen sections). The whole area of each thin section was investigated with 0.3 mm spaces between points and 0.9 mm between traverses. Microscope magnification for this work was 312.5 x. Mineral grains less than 50 μm apparent diameter were counted as matrix. Results are reported in Table S1.

2) The same thin sections were then subjected to a systematic analysis of the properties of quartz grains; e.g., unshocked, shocked (with planar fractures [PFs] and PDFs), number of sets of PF and PDF, respectively, presence of PDF decoration, toasted appearance, etc (Table S2). Only quartz grains with sizes larger than 50 μm were examined along traverses spaced at 1.2 mm. For each thin section, about 500 quartz grains were investigated.

3) The crystallographic orientations of 1056 PDF sets in 602 PDF-bearing quartz grains were measured by U-stage, on seventeen thin sections of MGW (no PDF were observed in quartz grains from sample KR8-125; depth = 451.2 m) following the methods described by, e.g., Engelhardt and Bertsch (*S4*), Stöffler and Langenhorst (*S5*), and Grieve et al. (*S6*). The number of measured PDF is restricted to the surface area that can be investigated with the U-stage (usually about one third of the section). The optic axis orientation and that of the pole to a PDF plane were determined, and PDF were indexed in a stereonet with the c-axis placed into the center (e.g., *S4*, *S5*). The PDF poles were indexed with Miller-Bravais indices (*hkl*) for quartz following techniques outlined

in, e.g., Engelhardt and Bertsch (*S4*) and Stöffler and Langenhorst (*S5*), and only between 0 and 5.6 rel% of all the measured sets in the different samples could not be indexed. To allow comparison between the different samples (without the influence of the number of unindexed PDFs planes on the proportion of the various orientations), the unindexed PDF planes were subtracted from the total number of measured PDFs for each sample. Data in absolute frequency percent (i.e., corrected for unindexed PDFs) are reported in Table S3. The reported data represent the totality of PDF orientations measured in all quartz grains, including the grains with 1, 2, 3, and 4 sets; to control the robustness of our data, absolute frequency of indexed PDFs was also recalculated using only measurements of PDF orientations measured in quartz grains with 2 sets and no significant differences were observed.

Supporting online text

Previous studies on shock pressure distribution in impact structures

In most previous studies of shock pressure distribution in impact structures (e.g., *S7–S11*), authors used a method similar to that developed by Grieve and Robertson (*S12*). This method derives average shock pressure values for a given sample based on the assignation of fixed values of pressure to each individual PDF orientation, namely, 7.5 GPa for PDF parallel to $c(0001)$, 10 GPa for PDF parallel to $\omega\{10\bar{1}3\}$, 14 GPa for PDF parallel to $\{22\bar{4}1\}$, $r/z\{10\bar{1}1\}$, and $\xi\{11\bar{2}2\}$, and 16 GPa for PDF parallel to $\pi\{10\bar{1}2\}$. Average shock pressure is then calculated on the basis of proportions of different PDF orientations.

A problem with this approach is that other typical crystallographic orientations of PDFs in shocked quartz (as $m\{10\bar{1}0\}$, $s\{11\bar{2}1\}$, $\rho\{21\bar{3}1\}$, $x\{51\bar{6}1\}$, $a\{11\bar{2}0\}$, etc.) (*S5*) are ignored, and it is not clear how these orientations of PDFs enter into the calculation of average pressure values. It is also not clear how co-existing orientations (e.g., c and π) enter these counting statistics – as these indicators of lower and moderate shock pressures may well form at the same pressure – in the example case more likely at the higher end of the range given by these two orientations. There are also studies that show that the onset of double orientation development is more likely at ca. 15 GPa (e.g., *S13*). In addition, these studies did not provide sufficient descriptions and characteristics of the investigated samples, when differences in lithology, texture, fabric, grain size, porosity, etc., in the investigated lithologies, as well as rheological contrasts between adjacent lithologies and/or different degrees of brittle deformation can significantly influence the development of PDFs in quartz. Furthermore, only limited numbers of quartz grains and only few PDF set orientations were measured, raising questions about how representative these results are.

Brief description of the Bosumtwi impact structure

The Bosumtwi impact structure, located in Ghana, West Africa, is a well-preserved, complex, young impact structure, with a pronounced rim and small central uplift (e.g., *S14–S15*). The structure has a rim-to-rim diameter of about 10.5 km. The crater, only 1.07 Myr old, was excavated in lower greenschist facies metasediments of the 2.1-2.2

Gyr Birimian Supergroup, and is now filled almost entirely by Lake Bosumtwi of 8 km diameter (S15; and references therein). In addition to earlier remote sensing and geophysical, as well as limited surface-based, studies, a recent international and multidisciplinary drilling project by the International Continental Scientific Drilling Program (ICDP) (see S16 for review) led to the recovery of two drill cores from the crater fill and underlying basement. Cores LB-07A and LB-08A (Fig. 1) were retrieved from the deep crater moat and the outer flank of the central uplift, respectively. The annular moat is filled with over 135 m of lithic and suevitic impact breccia. A well-defined, faulted, collapsed central uplift occurs near the north-central part of the crater (S17). The central uplift, composed of metasedimentary rocks overlain by about 25 m of fallback impact breccia (S1, S18), reaches ~130 m above the crater moat and is ~1.9 km wide (S17).

Geological setting and stratigraphy of drill core LB-08A

As noted above, the Bosumtwi impact structure was mostly excavated in lower greenschist-facies supracrustal rocks of the Birimian Supergroup, an assemblage of metasedimentary rocks that comprise phyllites, meta-tuffs, meta-graywackes, quartzitic meta-graywackes, schists, shales, and slates (e.g., S15).

In this study we focus on core LB-08A (Fig. 1), which was recovered from 235.6 to 451.33 m, representing 215.7 m of core with a diameter of 6 cm. All depths indicated are depths below lake level. Initial descriptions of drill core LB-08A were reported by Deutsch et al. (S18) and Ferrière et al. (S1). According to these authors, core LB-08A can be subdivided into two parts: the uppermost 25 m, composed of polymict lithic impact breccia (clast-supported) intercalated with suevite units, and the lower part composed of fractured/brecciated metasedimentary rocks between 262 to 451 m, dominated by MGW units alternating with phyllite and slate and intersected by a few suevite dikelets. The upper 25 m of the core most likely represent fallback impact breccia superimposed on the basement rocks that have been shocked and then uplifted during impact crater formation (S1).

In comparison, core LB-07A, drilled only 615 m northwest of the drill site for core LB-08A (Fig. 1), is composed of a thick section of impact breccia (333.4–470.6 m depth) overlying basement rocks (mostly metapelites and some MGW), from 470.6 m to the total drilling depth of 545.1 m (S19).

Petrographic investigations

1) Modal analyses:

The modal compositions for the MGW samples are reported in volume% in Table S1. Quartz comprises an overall estimated 43 vol%, and typically, feldspar (K-feldspar and plagioclase) grains/fragments account for about 30 vol%, with some variation between samples (see Table S1). The matrix represents, on average, about 10 vol%, with significant variations, from 2.7 vol% (in KR8-125) to 26.5 vol% (in KR8-36). In addition, MGW contains (with decreasing abundance): chlorite, calcite, muscovite, opaque minerals (mostly pyrite), chert clasts, biotite, epidote, amphibole, sphene, apatite, zircon, and allanite (Table S1). Chlorite is generally present as a secondary alteration

product after biotite. No specific or discernible trends with depth in the relative abundance of the different populations of minerals have been observed.

2) Properties of quartz grains and occurrence of shocked quartz:

Ferrière et al. (S1) noted that most of the MGW from the basement (i.e., in core LB-08A) is shocked (occurrence of PFs and PDFs in quartz grains). Quartz occurs mostly as single crystals (rarely as polycrystalline clasts) and frequently shows micro-fractures and undulatory extinction. Our investigations of the properties of ~9000 quartz grains in eighteen MGW samples (see Table S2) indicate that quartz grains with undulatory extinction are irregularly distributed through the central uplift interval. Shocked quartz grains observed in MGW display PFs and PDFs (1, 2, 3, and rarely 4 sets; Fig. S1); about 50 rel%, on average, of the PDFs are decorated with numerous small fluid inclusions (Table S2). Traditionally decorated PDFs are considered “secondary” features, formed by annealing and aqueous alteration of non-decorated amorphous PDFs (e.g., S6, S20). In some instances, the quartz grains have a grayish brown appearance (Fig. S1c), with patches containing micrometer-sized fluid inclusions (too small to be resolved with the petrographic microscope); this has been described as “toasted appearance” (S21, S22). About 20 rel% of the shocked quartz grains show this “toasted appearance” (Table S2). The abundance of decorated PDFs and of toasted quartz grains does not seem to be dependent on depth. However, the relative abundances of quartz grains with decorated PDFs and of those with “toasted appearance” indicate a relatively good correlation ($r = 0.80$; Fig. S2). On the other hand, quartz grains that display mosaicism occur mostly in samples from the top of the core; up to 34 % of the shocked quartz grains show mosaicism in sample KR8-030 (Table S2). According to Stöffler and Langenhorst (S5), mosaicism is defined as a “highly irregular mottled optical extinction pattern” and is “distinctly different from undulatory extinction”. Mosaicism results of the distortion of the lattice into small domains that are rotated by low angles against each other; it is an indicator of pressure on the order of ~30 GPa (e.g., S5).

It is obvious from Table S2 that the number of shocked quartz grains decreases with increasing depth; Fig. S2 shows a good correlation between the number of shocked quartz grains and depth ($r = -0.85$). About 60 % of the quartz grains are shocked in the samples from between 270 and 275 m depths, about 25 vol% in the samples from between 350 and 370 m depths, and less than 15 vol% in the samples from the last 20 m of the core (Fig. 2; Table S2). Concurrently, a decrease of the abundance of PDF sets per grain with depth is observed (Fig. 3; Table S2). The higher abundance of PDF sets per grain is partly caused by the presence of quartz grains with 3 to 4 sets of PDFs which occur only in samples from the uppermost part of the core (Table S2).

3) Orientations of planar deformation features in quartz:

A large proportion, from 69 to 100 rel% (for the various thin sections; see Table S3), of all the poles to the PDF planes measured are oriented at ~23° to the c-axis, corresponding to the $\omega_{\{10\bar{1}3\}}$ orientation. Only a small proportion of basal PDF [parallel to (0001)] was found, typically less than 5 rel% per section, with the notable exception of two samples, KR8-85 and KR8-89, from between 390 and 400 m, in which up to 27 rel% of basal PDFs occur (Table S3). However, about 50% of the basal PDFs measured in these two samples occur in association with other PDF orientations in the same quartz

grain; similar proportion, ~40% in average, of the basal PDFs measured in all the other samples occur in association with other PDF orientations in the same grain. Other measured PDF orientations, which rarely occur at more than 5 rel% per section, include (in relative order of decreasing abundance) $\rho\{2\bar{1}3\}$, $\pi\{10\bar{1}2\}$, $x\{5\bar{1}6\}$, $r/z\{10\bar{1}1\}$, $s\{11\bar{2}1\}$, $\xi\{11\bar{2}2\}$, $m\{10\bar{1}0\}$, and $a\{11\bar{2}0\}$. These orientations do not represent more than 1.5 rel% of all measurements (see Table S3).

PDF sets not observable under horizontal stage examination are visible when using a U-stage. Figure 3 clearly shows the systematically higher average number of PDF sets per grains (denoted N) when determined with the U-stage. Those higher N values closely follow the same trend as the values of N directly calculated from our analysis of the properties of quartz grains systematic analyses (Fig. 3); this systematic shift in the N values, on average, 28 ± 9 rel% higher when determined with the U-stage, confirms that the results of our U-stage measurements are statistically representative of the complete thin sections (even though only a restricted part of the section can be investigated using the U-stage). For comparison, the abundance of PDF sets as determined using the U-stage is reported in the bottom part of the Table S2. In U-stage observations, quartz grains with 2 PDF sets account for ~50 rel%, whereas they represent only one third of the total in horizontal stage examinations (see Table S2).

Numerical modeling

Numerical modeling allows to record any desirable variable for any location within an impact crater and for all times during the crater formation process (e.g., S23). Here we used the Simplified Arbitrary Lagrangian-Eulerian code, version B (SALEB; S24), as also used by Artemieva et al. (S25), but with an extended range of model parameter variation. In contrast to Artemieva et al. (S25), we made a direct parametric fit of our model to the observed crater geometry, without usage of scaling relations for the crater size. In addition, we made the fit to the actual position of the central uplift, below the rim level, without assumption of bulking.

Calculations were done for a vertical impact of a spherical projectile. To model the mechanical properties of the projectile and of the Bosumtwi target (projectile is assumed to be made of the same material as the target), we used the tabulated ANEOS equation of state for Westerly granite (S26) and the Tillotson EOS fitted to the granite Hugoniot for the range below 100 GPa. In addition, available ANEOS equations of state for dunite and calcite were also tested. Acoustic fluidization (AF) model parameters (see Table S4) were tuned to reproduce the depth and width of the central uplift.

Our best model was obtained for the model parameters listed in Table S4. Model crater profiles for two model runs (of a total of about two dozen) compared to the observed crater cross-section of the Bosumtwi crater are presented in Fig. S3. Each model run starts with the impact and stops 75 seconds after the impact. Mass-less Lagrangian tracers imbedded into each cell (with sizes of 12×12 m or of 14×14 m) record shock pressure and the material motion through the Eulerian grid. The projectile has a resolution of 27 cells per projectile radius (CPPR) for models with an impact velocity of 10 km s^{-1} and of 18 CPPR for models with an impact velocity of 20 km s^{-1} .

After modeling, tracers in the vicinity of the exact location of the two drill holes were identified, allowing the reconstruction of their initial positions. As the model is too

crude to exactly represent the real rock displacements, we used a comparative approach, comparing model results and observations. All tracers in a zone of about 20 m (comparable with the cell size of 12×12 m), at the correct radial distances from the crater center (0.48 and 1.1 km for LB-08A and LB-07A, respectively), were listed, and finally, the position of the top of the “model core” was defined by the maximum recorded shock pressure of 30 GPa (pressure estimate based on our petrographic investigations). The bottom part of the “model cores” was defined by a tracer identified 200 m below the position of the 30 GPa level in the “model core” for core LB-08A, and at about 100 m below the 30 GPa level for core LB-07A. Then, the initial position of these tracers was plotted (Fig. 4), showing which layers of the target were sampled by the “model cores”.

To estimate the level of confidence of our modeling, several dozen model runs were calculated, varying the parameters of the target material as well as the impact velocity. We find that our modeling is robust, as for all model runs the same relative positions of rocks in cores LB-07A and LB-08A were observed. We have also noted that the shock pressure decay is slightly different for low- and high-velocity projectiles (Fig. S4).

Supporting figures

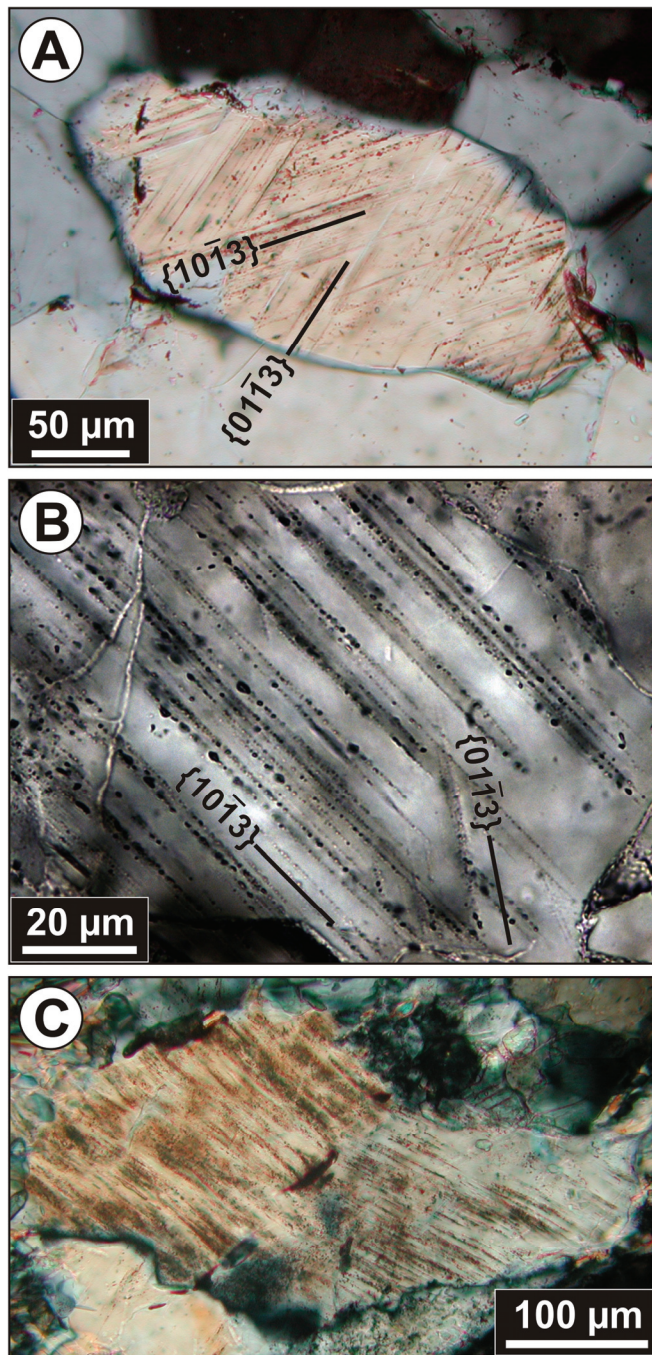


Fig. S1. Microphotographs of shocked quartz grains in meta-graywacke. a) Quartz grain with 2 sets of PDFs. Sample KR8-067; depth = 356.59 m (cross-polarized light). b) Decorated (with numerous tiny fluid inclusions) PDFs in a quartz grain (2 sets). Sample KR8-056; depth = 326.78 m (plane-polarized light). c) Typical quartz grains showing the toasted appearance. Sample KR8-098; depth = 410.74 m (cross-polarized light).

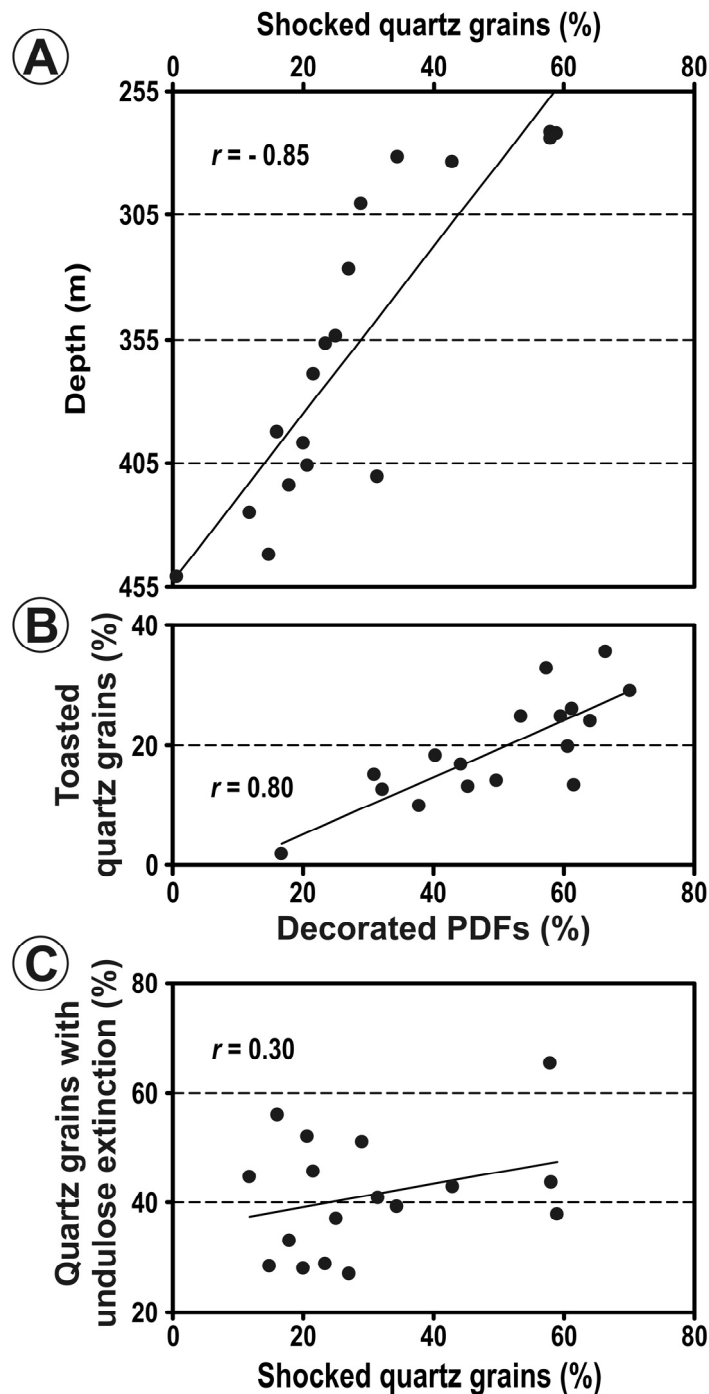


Fig. S2. Binary diagrams showing the degree of correlation between: a) the location of the samples in LB-08A drill core (i.e., depth; in meters) and the relative abundance of shocked quartz grains (i.e., quartz grains with PFs and PDFs; in %); b) the relative abundance of toasted quartz grains and those with decorated PDFs (in %); c) the relative abundance of quartz grains that show undulose extinction and the abundance of shocked quartz grains (in %). No correlation is observed between the proportion of quartz grains with undulose extinction and the proportion of shocked quartz grains.

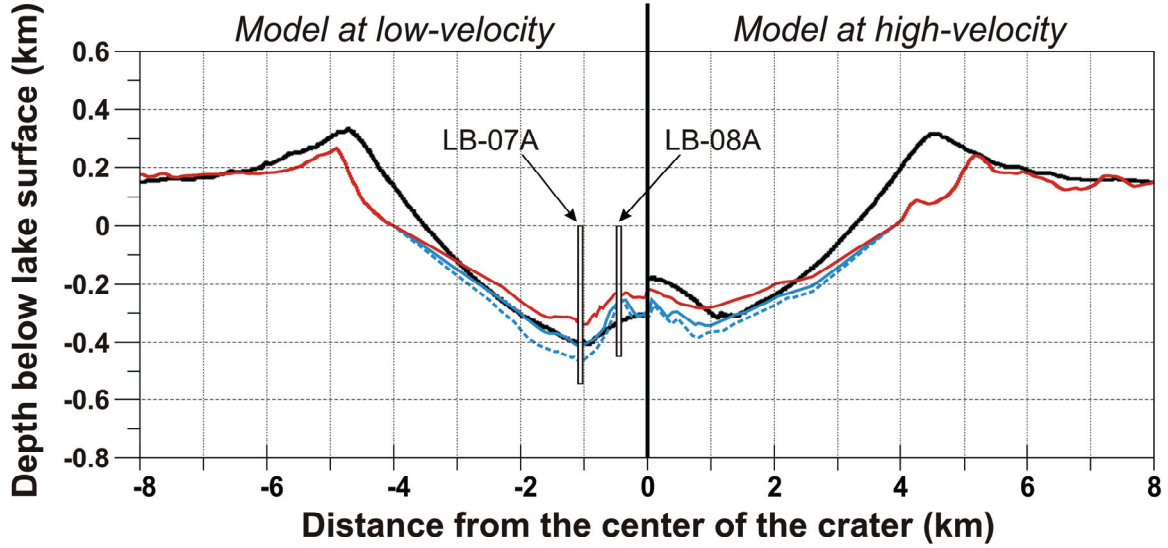


Fig. S3. Model crater profiles (black curves; using ANEOS granite equation of state for target and projectile) versus observed (i.e., actual) crater profile (red and solid blue lines for the apparent and true crater profiles, respectively, and dashed blue line for the lower limit of the monomict impact breccia). Note the difference between modeled and actual crater profile around the rim, which can be explained by post-impact erosion. Models of impact at low-velocity (left, $v_{\text{imp}} = 10 \text{ km s}^{-1}$, $D_{\text{proj}} = 0.648 \text{ km}$, $\delta = 2630 \text{ kg m}^{-3}$) and at high-velocity (right, $v_{\text{imp}} = 20 \text{ km s}^{-1}$, $D_{\text{proj}} = 0.432 \text{ km}$, $\delta = 2630 \text{ kg m}^{-3}$) are compared. In both runs, residual friction (μ) = 0.4, the fraction of the maximum particle velocity (C_{vib}) = 0.15, and decay time (Γ_{dec}) = 6 s. The ratio of projectile diameters is chosen to keep the “late stage equivalency” $D_{\text{proj}} \times v_{\text{imp}}^{0.58}$ constant. In both runs the apparent crater diameter is about 9 km. Location of boreholes LB-07A and LB-08A is given.

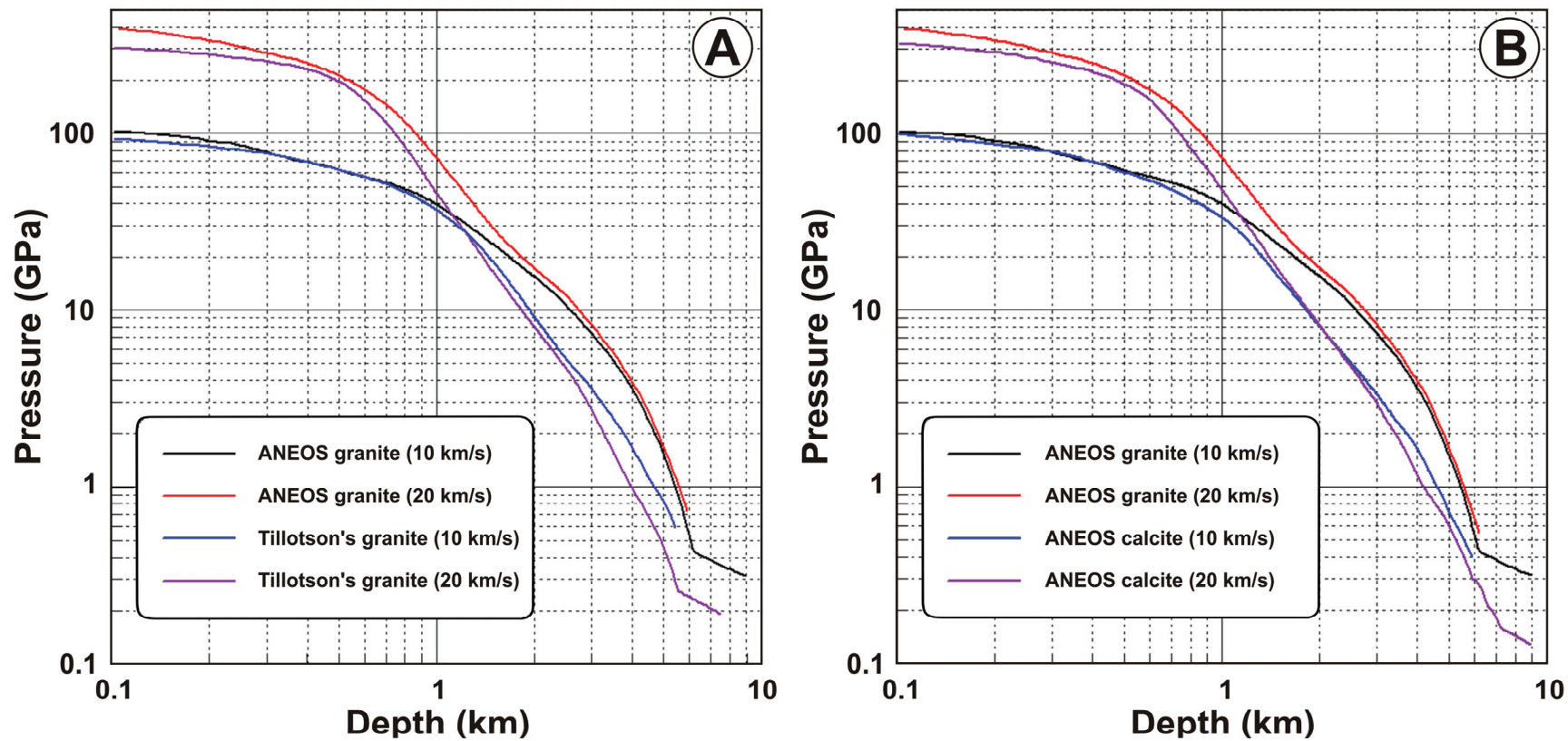


Fig. S4. Comparison of the shock pressure decay along the vertical center line for different materials and impact velocities. In all cases, targets and projectiles are made of the same material. The ANEOS granite case is shown as a reference in comparison with (a) Tillotson's EOS for granite and (b) ANEOS calcite. The 10 km s^{-1} projectiles have diameters of 0.648 km, whereas 20 km s^{-1} projectiles have diameters of 0.432 km.

Supporting tables

Table S1. Modal analyses (in vol%) by optical microscopy on thin sections of eighteen meta-graywacke samples from the basement, drill core LB-08A, Bosumtwi impact structure^a.

Sample (KR8-#)	29	30	31	36	37	45	56	66	67	71	85	89	96	98	101	109	119	125	Average	
Depth (m)	271.4	272.0	274.0	281.3	283.5	300.4	326.8	354.0	356.6	369.0	392.7	397.3	406.3	410.7	414.3	425.2	441.9	451.2		
Quartz	46.4	43.5	40.5	34.9	42.5	37.3	45.6	39.8	50.9	44.9	35.0	46.9	37.0	43.4	46.0	45.7	52.4	42.2	43.0	
Feldspar	K	23.7	27.8	18.9	22.3	14.4	20.3	15.4	22.6	17.1	16.8	24.4	10.3	21.2	18.7	18.5	12.7	15.3	17.6	18.8
	P	10.8	10.9	13.7	8.6	6.5	12.9	11.7	8.2	9.0	13.5	13.7	9.8	13.1	12.2	14.8	11.7	9.1	14.1	11.3
	Total	34.5	38.7	32.5	31.0	20.8	33.2	27.1	30.8	26.1	30.3	38.1	20.0	34.2	31.0	33.2	24.4	24.4	31.7	30.1
Matrix ^b	6.5	6.0	7.4	26.5	17.6	13.3	10.3	12.8	6.1	4.3	14.3	15.1	16.6	11.6	7.6	8.1	5.5	2.7	10.7	
Biotite	n.d.	n.d.	n.d.	x	x	x	x	x	x	n.d.	n.d.	x	x	n.d.	n.d.	3.9	x	x	0.3	
Chlorite	4.7	3.2	9.4	1.7	10.4	2.9	4.2	7.5	4.6	8.5	6.4	3.5	3.2	2.4	6.2	5.1	7.3	8.8	5.6	
Muscovite	1.3	2.2	2.3	1.4	4.2	1.5	5.1	2.9	3.5	2.1	2.3	3.3	1.4	1.7	x	x	0.9	3.3	2.2	
Chert	0.6	1.7	1.1	n.d.	1.2	1.5	1.1	x	1.0	1.8	0.6	0.6	n.d.	1.6	n.d.	1.4	1.6	1.7	1.0	
Calcite	3.6	2.5	1.2	2.2	x	2.9	0.8	3.0	4.8	3.0	0.6	5.1	1.9	0.8	1.2	2.0	5.8	7.2	2.7	
Opaque minerals	1.7	1.5	4.1	1.9	n.d.	1.8	1.0	2.1	1.1	2.0	1.8	3.2	1.4	2.5	0.5	1.0	1.9	1.9	1.7	
Other minerals ^c	0.6	0.8	1.5	x	2.7	5.3	4.5	0.7	1.8	3.1	1.0	2.1	3.9	5.0	5.0	7.9	x	0.5	2.6	
Total Counts	1413	1827	1352	1150	1204	714	708	1155	909	1039	877	779	567	827	644	692	694	754	961	

^aK = alkali feldspar; P = plagioclase; x = traces (<0.5 vol%); n.d. = none detected.

^bMatrix represents all grains smaller than 50 µm.

^cIncluding epidote, amphibole, sphene, apatite, zircon, and allanite (in order of decreasing abundance).

Table S2. Results from point-counting of quartz grain properties in eighteen meta-graywacke samples from the basement, drill core LB-08A, Bosumtwi impact structure, in comparison with PDF set abundances determined using universal stage^a.

Sample (KR8-#)	29	30	31	36	37	45	56	66	67	71	85	89	96	98	101	109	119	125	Total	
Depth (m)	271.4	272.0	274.0	281.3	283.5	300.4	326.8	354.0	356.6	369.0	392.7	397.3	406.3	410.7	414.3	425.2	441.9	451.2	8991	
Grains counted	508	521	566	520	490	501	533	520	564	519	511	556	374	522	461	476	407	442	8991	
% relative to total No. of quartz grains within sample																				
Unshocked	42	41	42	66	57	71	73	75	77	78	84	80	79	69	82	88	85	99		
Shocked	58	59	58	34	43	29	27	25	23	22	16	20	21	31	18	12	15	<1		
% relative to total No. of shocked quartz grains within sample																				
PF	9.2	9.4	10.4	15.1	16.7	23.4	24.3	30.0	24.2	29.5	40.2	34.2	36.4	22.0	52.4	46.4	65.0	100		
PDF	90.8	90.6	89.6	84.9	83.3	76.6	75.7	70.0	75.8	70.5	59.8	65.8	63.6	78.0	47.6	53.6	35.0	n.d.		
% relative to total No. of quartz grains with PDFs examined within sample																				
PDF sets	1	43	38	54	68	62	72	68	63	71	78	67	58	69	68	74	57	81	N/A	Average 64.2
	2	51	46	42	31	37	28	32	37	28	22	33	41	31	32	26	43	19	N/A	34.0
	3	6	14	3	<1	2	n.d.	n.d.	n.d.	1	n.d.	n.d.	1	n.d.	n.d.	n.d.	n.d.	n.d.	N/A	1.6
	4	<1	1	n.d.	N/A	0.1														
Avg. No. PDF sets/grain	1.65	1.78	1.49	1.32	1.40	1.28	1.32	1.37	1.30	1.22	1.33	1.44	1.31	1.32	1.26	1.43	1.19	N/A		
% relative to total No. of shocked quartz grains within sample																				
Decorated PDF	53	31	66	50	60	64	70	45	61	62	40	61	44	57	38	32	17	N/A	Average 50	
Toasted	25	15	36	14	25	24	29	13	20	13	18	26	17	33	10	13	2	N/A	20	
Undulose extinction	65	38	44	39	43	51	27	37	29	46	56	28	52	41	33	45	28	N/A	41	
Grain mosaicism	15	34	19	1	9	<1	2	2	2	2	2	<1	n.d.	1	n.d.	4	n.d.	N/A		
No. PDF sets; % relative to total No. of quartz grains with PDFs examined within sample; determined using universal stage																				
PDF sets	1	21	24	21	30	26	42	38	41	47	46	45	46	41	47	40	48	42	N/A	Average 37.9
	2	52	48	66	65	59	44	47	48	43	49	45	49	41	47	50	44	49	N/A	49.7
	3	24	21	13	5	13	12	13	11	11	5	10	6	17	6	10	8	9	N/A	11.4
	4	3	7	n.d.	n.d.	3	2	2	n.d.	N/A	1.0									
Avg. No. PDF sets/grain	2.10	2.10	1.91	1.75	1.92	1.74	1.79	1.70	1.64	1.59	1.66	1.60	1.76	1.58	1.70	1.60	1.67	N/A		

^aQuartz grains with diameter < 50 µm were not counted.
Abbreviations: n.d. = none detected; N/A = not applicable.

Table S3. Indexed PDF crystallographic orientations in quartz grains in meta-graywacke samples from the basement section of drill core LB-08A^a. Data given as absolute frequency values (recalculated to 100% without unindexed PDF orientations)^b.

Sample	Depth (m)	PDF crystallographic orientations										Total number of measured sets
		c {0001}	ω {10 $\bar{1}$ 3}	π {10 $\bar{1}$ 2}	r, z {10 $\bar{1}$ 1}	m {10 $\bar{1}$ 0}	ξ {11 $\bar{2}$ 2}	s {11 $\bar{2}$ 1}	a {11 $\bar{2}$ 0}	x {51 $\bar{6}$ 1}	ρ {21 $\bar{3}$ 1}	
KR8-29	271.43	1.7	93.3	3.3	n.d.	n.d.	1.7	n.d.	n.d.	n.d.	n.d.	60
KR8-30	272.00	n.d.	87.9	3.4	5.2	n.d.	1.7	1.7	n.d.	n.d.	n.d.	58
KR8-31	273.99	n.d.	90.7	1.2	n.d.	1.2	n.d.	2.3	n.d.	2.3	2.3	86
KR8-36	281.32	2.9	88.2	n.d.	n.d.	n.d.	n.d.	2.9	1.5	1.5	2.9	68
KR8-37	283.50	n.d.	95.8	1.4	1.4	n.d.	1.4	n.d.	n.d.	n.d.	n.d.	71
KR8-45	300.41	n.d.	100	n.d.	n.d.	n.d.	n.d.	n.d.	n.d.	n.d.	n.d.	75
KR8-56	326.78	5.0	83.8	1.3	1.3	n.d.	1.3	n.d.	n.d.	1.3	6.3	80
KR8-66	353.95	6.7	88.9	n.d.	n.d.	2.2	n.d.	2.2	n.d.	n.d.	n.d.	45
KR8-67	356.59	2.6	86.8	1.3	5.3	n.d.	n.d.	1.3	n.d.	1.3	1.3	76
KR8-71	368.97	9.1	76.4	n.d.	1.8	n.d.	n.d.	1.8	n.d.	7.3	3.6	55
KR8-85	392.65	27.1	68.8	2.1	n.d.	n.d.	n.d.	n.d.	n.d.	n.d.	2.1	48
KR8-89	397.30	18.9	77.4	1.9	n.d.	n.d.	n.d.	n.d.	n.d.	1.9	n.d.	53
KR8-96	406.31	n.d.	92.0	n.d.	n.d.	n.d.	n.d.	2.0	n.d.	4.0	2.0	50
KR8-98	410.74	1.8	94.7	n.d.	1.8	n.d.	1.8	n.d.	n.d.	n.d.	n.d.	57
KR8-101	414.28	n.d.	93.9	6.1	n.d.	n.d.	n.d.	n.d.	n.d.	n.d.	n.d.	33
KR8-109	425.24	2.6	87.2	n.d.	2.6	n.d.	n.d.	2.6	n.d.	2.6	2.6	39
KR8-119	441.87	1.5	97.1	n.d.	n.d.	n.d.	n.d.	n.d.	n.d.	n.d.	1.5	68
All samples combined		4.7	88.4	1.3	1.1	0.2	0.5	1.0	0.1	1.3	1.4	1022

^aMethod described in, e.g., Engelhardt and Bertsch (S4), Stöfler and Langenhorst (S5), and Grieve et al. (S6).

^bRecalculation without unindexed PDF orientations allows comparison between the different samples; from 0 to 5.5 rel% of the measured PDF orientations could not be indexed.

n.d. = none detected.

Table S4. Main parameters used in the acoustic fluidization (AF) model.

Equation of state	ANEOS granite	Tillotson EOS granite
Friction coefficient of totally damaged material	0.4	0.55
AF model switch on time, s	3	4
AF model decay time, s	6	6.4
AF model limiting velocity, m.s ⁻¹	100	300

Supporting references

- S1. L. Ferrière, C. Koeberl, W. U. Reimold, *Meteorit. Planet. Sci.* **42**, 611–633 (2007).
- S2. R. C. Emmons, *The Universal Stage* (GSA Memoir **8**, GSA, New York, 1943).
- S3. F. Chayes, *Am. Mineral.* **34**, 1–11 (1949).
- S4. W. v. Engelhardt, W. Bertsch, *Contrib. Mineral. Petrol.* **20**, 203–234 (1969).
- S5. D. Stöffler, F. Langenhorst, *Meteorit. Planet. Sci.* **29**, 155–181 (1994).
- S6. R. A. F. Grieve, F. Langenhorst, D. Stöffler, *Meteorit. Planet. Sci.* **31**, 6–35 (1996).
- S7. P. B. Robertson, R. A. F. Grieve, in *Impact and explosion cratering*, D. J. Roddy, R. O. Pepin, R. B. Merrill, Eds. (Pergamon Press, New York, 1977), pp. 687–702.
- S8. L. V. Sazonova, N. N. Karotaeve, G. Y. Ponomarev, A. I. Dabizha, in *Impactits*, A. A. Marakushev, Ed. (Moscow State University, Moscow, 1981), pp. 93–133 (in Russian).
- S9. R. A. F. Grieve, J. M. Coderre, P. B. Robertson, J. Alexopoulos, *Tectonophysics* **171**, 185–200 (1990).
- S10. V. I. Fel'dman, L. V. Sazonova, S. I. Kotel'nikov, *Dokl. Akad. Nauk SSSR* **349**, 658–660 (1996).
- S11. B. O. Dressler, V. L. Sharpton, B. C. Schuraytz, *Contrib. Mineral. Petrol.* **130**, 275–287 (1998).
- S12. R. A. F. Grieve, P. B. Robertson, *Contrib. Mineral. Petrol.* **58**, 37–49 (1976).
- S13. A. R. Huffman, W. U. Reimold, *Tectonophysics* **256**, 165–217 (1996).
- S14. C. A. Scholz *et al.*, *Geology* **30**, 939–942 (2002).
- S15. C. Koeberl, W. U. Reimold, *Yearb. Austrian Geol. Surv.* **145**, 31–70 (2005).
- S16. C. Koeberl *et al.*, *Meteorit. Planet. Sci.* **42**, 483–511 (2007).
- S17. C. A. Scholz, T. Karp, R. P. Lyons, *Meteorit. Planet. Sci.* **42**, 549–560 (2007).
- S18. A. Deutsch, S. Luetke, V. Heinrich, *Meteorit. Planet. Sci.* **42**, 635–654 (2007).
- S19. L. Coney, R. L. Gibson, W. U. Reimold, C. Koeberl, *Meteorit. Planet. Sci.* **42**, 569–589 (2007).
- S20. H. Leroux, *Meteorit. Planet. Sci.* **40**, 1347–1352 (2005).
- S21. N. M. Short, D. P. Gold, *GSA Spec. Pap.* **302**, 245–265 (1996).
- S22. J. Whitehead, J. G. Spray, R. A. F. Grieve, *Geology* **30**, 431–434 (2002).
- S23. G. S. Collins, H. J. Melosh, B. A. Ivanov, *Meteorit. Planet. Sci.* **39**, 217–231 (2004).
- S24. The original code was developed at Los Alamos Nat. Lab by A.A. Amsden *et al.*, *LAL Report LA-8095* (1980). The code has been advanced to treat multimaterial cells with Eulerian advection by B. Ivanov, *LPSC XXXIII*, abs. #1286 (2002). Material strength models were described by Collins *et al.*, *Meteorit. Planet. Sci.* **34**, 217–31 (2004), the acoustic fluidization model by Wünnemann and Ivanov,

- Planet. Space Sci.* **51**, 831–845 (2003), and verification of the code by modeling of 3 very large terrestrial impact craters was presented by B. Ivanov, *Solar Sys. Res.* **39**, 381–409 (2005).
- S25. N. Artemieva, T. Karp, B. Milkereit, *Geochem., Geophys., Geosyst.* **5**, doi:10.1029/2004GC000733 (2004).
- S26. E. Pierazzo, A. M. Vickery, H. J. Melosh, *Icarus* **127**, 408–423 (1997).